RSC Advances

PAPER

View Article Online
View Journal | View Issue

Cite this: *RSC Adv.*, 2021, **11**, 32269

X-ray absorption spectroscopy of exemplary platinum porphyrin and corrole derivatives: metal- *versus* ligand-centered oxidation†

Benjamin D. Matson,[a] Kolle E. Thomas,[b] Abraham B. Alemayehu,[b] Abhik Ghosh *[a] and Ritimukta Sarangi *[a]

A combination of Pt L_3-edge X-ray absorption spectroscopy (EXAFS and XANES) and DFT (TPSS) calculations have been performed on powder samples of the archetypal platinum porphyrinoid complexes $Pt^{II}[TpCF_3PP]$, $Pt^{IV}[TpCF_3PP]Cl_2$, and $Pt^{IV}[TpCF_3PC](Ar)(py)$, where $TpCF_3PP^{2-}$ = *meso*-tetrakis(*p*-trifluoromethylphenyl)porphyrinato and $TpCF_3PC^{3-}$ = *meso*-tris(*p*-trifluoromethylphenyl)corrolato. The three complexes yielded Pt L_3-edge energies of 11 566.0 eV, 11 567.2 eV, and 11 567.6 eV, respectively. The 1.2 eV blueshift from the Pt(II) to the Pt(IV) porphyrin derivative is smaller than expected for a formal two-electron oxidation of the metal center. A rationale was provided by DFT-based Hirshfeld which showed that the porphyrin ligand in the Pt(IV) complex is actually substantially oxidized relative to that in the Pt(II) complex. The much smaller blueshift of 0.4 eV, going from $Pt^{IV}[TpCF_3PP]Cl_2$, and $Pt^{IV}[TpCF_3PC](Ar)(py)$, is ascribable to the significantly stronger ligand field in the latter compound.

Received 14th August 2021
Accepted 23rd September 2021

DOI: 10.1039/d1ra06151h

rsc.li/rsc-advances

Introduction

Platinum, a renowned transition metal,[1,2] has long been a cornerstone of the field of catalysis. In the same vein, over the last half-century, cisplatin and related Pt(II) complexes have emerged as a mainstay of cancer chemotherapy, accounting for some 40% of all such treatment.[3–5] To avert off-target reactions and side effects of Pt(II) complexes, Pt(IV) complexes are also being actively studied as prodrugs, since they can generate the active cytotoxic Pt(II) drugs *via* intracellular reduction at their target sites.[6] In yet a third domain, Pt(II) porphyrins played an important role in Martin Gouterman's optical taxonomy of porphyrin derivatives[7] and, as strongly phosphorescent, oxygen-sensing materials, they famously found applications as pressure-sensitive paints on airplane wings.[8,9] Platinum(IV) porphyrins have also been known for many years.[10,11] Much more recently, Pt(IV) corroles have been synthesized,[12] albeit in poor yields, and found to exhibit near-IR phosphorescence under ambient conditions.[13,14] Given the importance of multiple oxidation states in Pt chemistry, X-ray absorption spectroscopy (XAS)[15,16] plays a major role in studies of Pt speciation in complex catalytic systems[17,18] and increasingly also in biological systems.[19] To assist such analyses, we carried out a Pt L_3 XAS study of a set of well-characterized Pt porphyrin and corrole derivatives. (Given their broad importance, there have been surprisingly few XAS and related measurements on porphyrin and corrole derivatives.[20–30]) The results, interpreted with density functional theory (DFT) calculations, provide detailed insights into the factors influencing the pre-edge shifts of Pt complexes.

Results and discussion

X-ray absorption spectroscopy (XAS)

Pt L_3-edge X-ray absorption spectroscopy (XAS), including X-ray absorption near-edge structure (XANES) and extended X-ray absorption fine structure (EXAFS) analysis, was performed on three complexes – $Pt^{II}[TpCF_3PP]$, $Pt^{IV}[TpCF_3PP]Cl_2$, and $Pt^{IV}[TpCF_3PC](Ar)(py)$ [$TpCF_3PP^{2-}$ = *meso*-tetrakis(*p*-trifluoromethylphenyl)porphyrinato, $TpCF_3PC^{3-}$ = *meso*-tris(*p*-trifluoromethylphenyl)corrolato, Ar = *m*-cyanophenyl, and py = pyridine; Fig. 1] – to interrogate their electronic structure and bonding parameters. (The choice of CF_3-substituted porphyrinoid ligands was prompted by the general expectation that the resulting complexes should be more resistant toward aerial oxidation and conducive to long-term storage.) The analyses were carried out on powdered samples. The three complexes yielded Pt L_3-edge energies of 11 566.0 eV, 11 567.2 eV, and 11 567.6 eV, respectively (Fig. 2). The Pt L_3-edge energies and intensities are sensitive to the charge (or electrostatic potential) and the number of empty 5d states, respectively, at the Pt center.[31,32] The increase in the L_3-edge energy and intensity of

[a]*Stanford Synchrotron Radiation Lightsource, SLAC National Accelerator Laboratory, Stanford University, Menlo Park, California 94025, USA. E-mail: abhik.ghosh@uit.no; ritis@slac.stanford.edu*

[b]*Department of Chemistry, UiT – The Arctic University of Norway, N-9037 Tromsø, Norway*

† Electronic supplementary information (ESI) available. See DOI: 10.1039/d1ra06151h

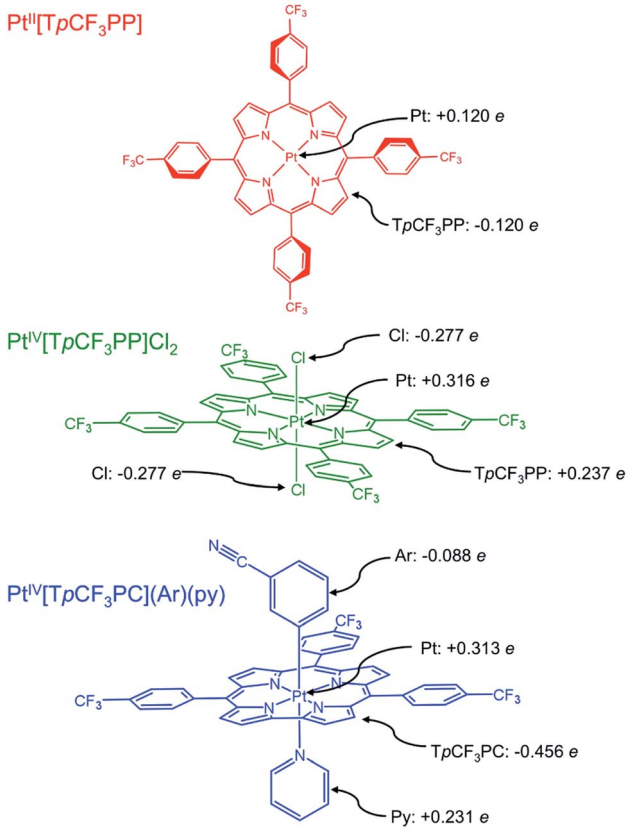

Fig. 1 Platinum porphyrin and corrole derivatives studied in this work, along with selected TPSS Hirshfeld charges.

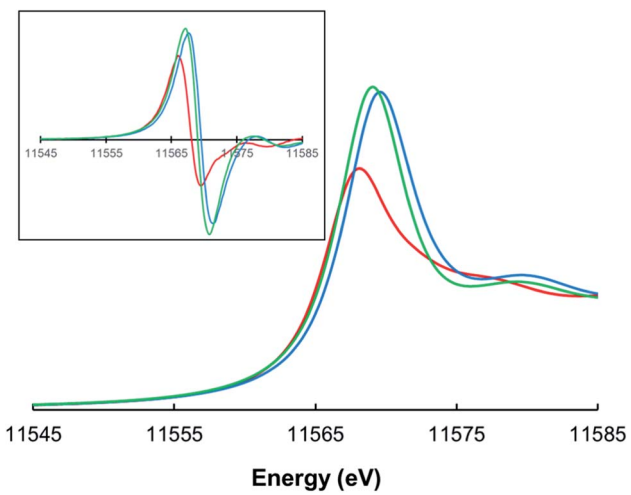

Fig. 2 Normalized Pt L_3-edge XAS spectra for $Pt^{II}[TpCF_3PP]$ (red), $Pt^{IV}[TpCF_3PP]Cl_2$ (green), and $Pt^{IV}[TpCF_3PC](Ar)(py)$ (blue). The inset depicts first derivative spectra.

$Pt^{IV}[TpCF_3PP]Cl_2$ when compared to $Pt^{II}[TpCF_3PP]$ is thus consistent with oxidation of the Pt center from, formally, Pt(II) to Pt(IV). The slight increase in the edge position of $Pt^{IV}[TpCF_3PC](Ar)(py)$, compared to $Pt^{IV}[TpCF_3PP]Cl_2$, is consistent with an oxidized species with an increase in the strength of the ligand field due to the $TpCF_3PC$, Ar and/or pyridine ligands. Support for this interpretation also comes from the approximately equal pre-edge intensities of $Pt^{IV}[TpCF_3PP]Cl_2$ and $Pt^{IV}[TpCF_3PC](Ar)(py)$, as expected for two low spin d^6 Pt(IV) species.

The bonding parameters of all three species were determined *via* EXAFS analysis (Fig. 3 and Table 1) and found to agree well with DFT optimized structures. Thus, the two Pt porphyrins $Pt^{IV}[TpCF_3PP]Cl_2$ and $Pt^{II}[TpCF_3PP]$ were found to exhibit similar Pt–N distances of 2.03 Å and 2.01 Å, respectively. The Pt–Cl distance in $Pt^{IV}[TpCF_3PP]Cl_2$ was determined to be 2.31 Å. EXAFS analysis of $Pt^{IV}[TpCF_3PC](Ar)(py)$ revealed 4 shortened Pt–N distances of 1.96 Å, as well as distances of 1.98 Å and 2.26 Å for the axial Pt–C_{Ph} and Pt–N_{py} bonds, respectively. These distances also served as proof of the chemical integrity of the samples under the conditions of the XAS experiments.

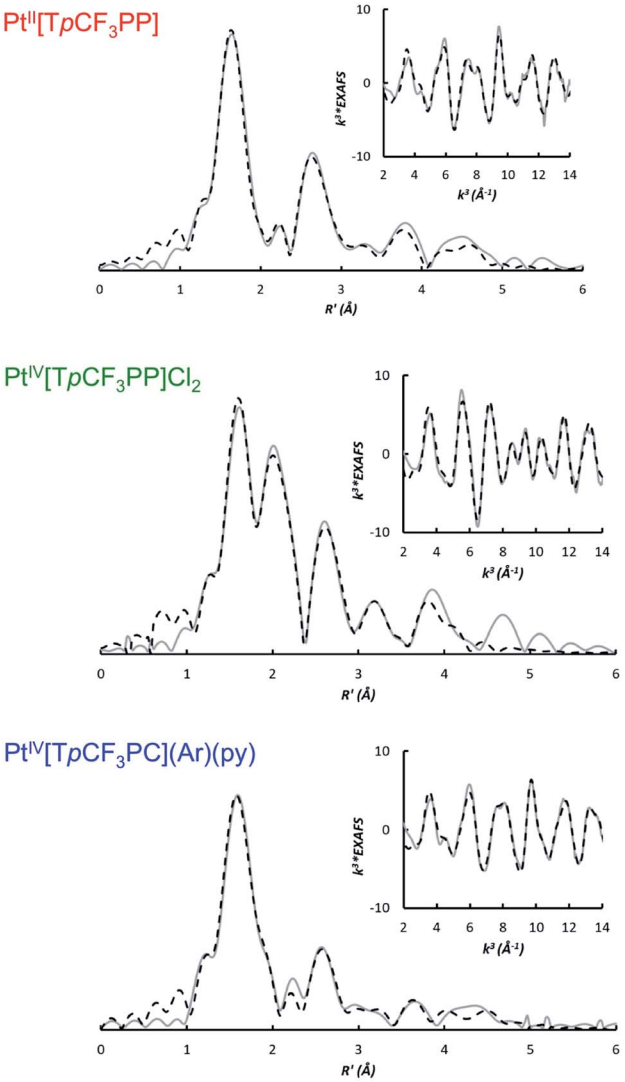

Fig. 3 Non-phase shift corrected Fourier transforms of the Pt L-edge EXAFS data (gray, solid) and corresponding fits (black, dashed) for $Pt^{II}[TpCF_3PP]$ (top), $Pt^{IV}[TpCF_3PP]Cl_2$ (middle), and $Pt^{IV}[TpCF_3PC](Ar)(py)$ (bottom). Insets show the EXAFS regions and their fits.

Table 1 Pt L-edge EXAFS curve-fitting results

Complex	Path	R^a (Å)	σ^{2b} (Å^2)	ΔE_0
$Pt^{II}[TpCF_3PP]$	4 Pt–N	2.01	388	10.56
	8 Pt–C_{pyr}	3.04	227	
	16 Pt–N–C_{pyr}	3.20	1688	
	4 Pt–C_{meso}	3.42	364	
	16 Pt–C_{meso}–C_{pyr}	3.91	385	
	16 Pt–C_{pyr}–C_{pyr}'	4.32	62	
	8 Pt–C_{meso}–C_{ph}	4.92	202	
$Pt^{IV}[TpCF_3PP]Cl_2$	4 Pt–N	2.03	214	9.25
	2 Pt–Cl	2.31	182	
	8 Pt–C_{pyr}	3.05	258	
	4 Pt–C_{meso}	3.39	389	
	16 Pt–N–Cl	3.78	214*	
	4 Pt–N–N′	4.02	846	
	16 Pt–N–C_{pyr}	4.31	214*	
$Pt^{IV}[TpCF_3PC](Ar)(py)$	4 Pt–N	1.96	211	7.46
	1 Pt–C_{ph}	1.98	211*	
	1 Pt–N_{py}	2.26	211*	
	6 Pt–C_{pyr}	2.96	211*	
	3 Pt–C_{meso}	3.31	211*	
	8 Pt–N–N_{py}	3.90	211*	
	8 Pt–N–C	4.18	184	
	6 Pt–C_{meso}–C	4.82	157	

[a] The estimated standard deviations for the distances are in order of ±0.02 Å. [b] The σ^2 values are multiplied by 10^5. A * indicates that the σ^2 value was linked to that of the Pt–N path.

Density functional theory

To shed additional light on the electronic structure of the three Pt species, DFT (TPSS[33]) calculations were performed with SARC-ZORA (Pt)[34] and def2-TZVP[35–37] basis sets. As noted above, the Pt L_3-edge blueshifts by 1.2 eV upon oxidation of $Pt^{II}[TpCF_3PP]$ to $Pt^{IV}[TpCF_3PP]Cl_2$. While this shift to higher energy is expected upon oxidation, the magnitude of the energy shift is significantly lower than expected for 2-e$^-$ oxidation, *i.e.*, Pt(II) to Pt(IV). Hirshfeld charges obtained from the calculations showed that both the Pt centers and $TpCF_3PP$ ligands are oxidized by an appreciable amount, when going from $Pt^{II}[TpCF_3PP]$ to $Pt^{IV}[TpCF_3PP]Cl_2$. In $Pt^{II}[TpCF_3PP]$, the charge on the Pt center is calculated to be +0.120*e* (*e* being the absolute value of the electronic charge) and, accordingly, the charge on the $TpCF_3PP$ ligand is −0.120*e* in the neutral species. By comparison, $Pt^{IV}[TpCF_3PP]Cl_2$ shows an increased charge on Pt (+0.316*e*) and $TpCF_3PP$ (+0.237*e*), with the two chlorido groups (−0.277*e* each) balancing out yield the neutral species. Taken together, these Hirshfeld charges suggest that the relatively small Pt L_3-edge blueshift upon oxidation of $Pt^{II}[TpCF_3PP]$ to $Pt^{IV}[TpCF_3PP]Cl_2$ reflects substantial oxidation of the $TpCF_3PP$ ligand (Δq = +0.357*e*), as well as, of course, the Pt center (Δq = +0.196*e*).

Further insight into the electronic structures came from visualization of the d-based frontier molecular orbitals (FMOs, Fig. 4–6). The 6-coordinate, d^6 species $Pt^{IV}[TpCF_3PP]Cl_2$ (Fig. 5) shows the expected d-manifold splitting in which the fully occupied, non-bonding d_{xy} orbital lies lowest in energy and a fully occupied, degenerate set of (d_{xz}, d_{yz})-derived π-nonbonding orbitals at a relative energy of +2.9 eV. Higher still in energy are the unoccupied σ* orbitals derived from d_{z^2} (+5.3 eV relative to d_{xy}) and $d_{x^2-y^2}$ (+6.1 eV relative to d_{xy}). Comparison of these FMOs to those of the structurally similar $Pt^{IV}[TpCF_3PC](Ar)(py)$ reveals some crucial differences in the bonding and ligand field strength of the associated ligands. Although the d-based FMOs appear in the same order in both

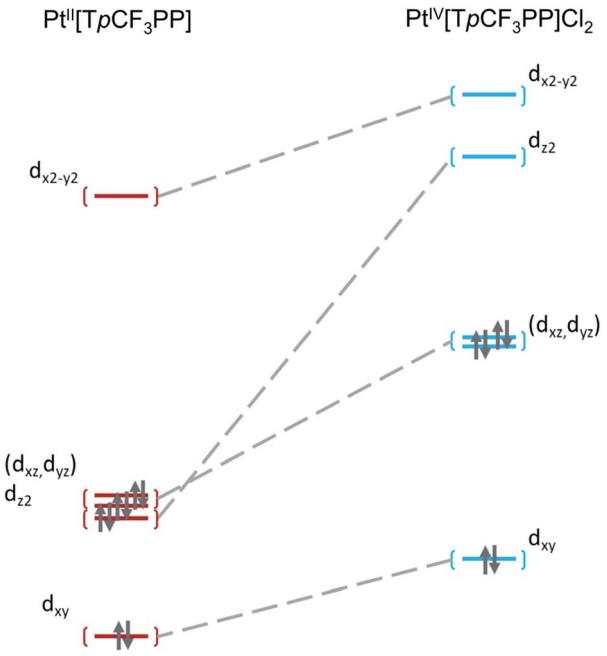

Fig. 4 Comparative Kohn–Sham (TPSS) d-orbital energy level diagrams for $Pt^{II}[TpCF_3PP]$ and $Pt^{IV}[TpCF_3PP]Cl_2$.

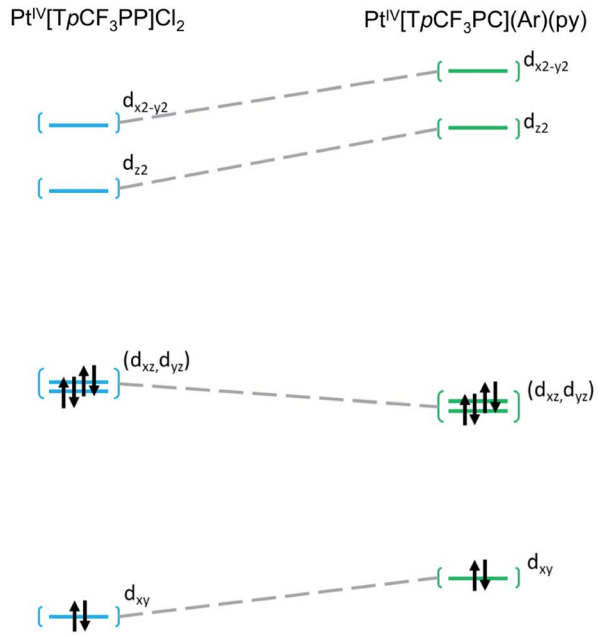

Fig. 5 Comparative Kohn–Sham (TPSS) d-orbital energy level diagrams for $Pt^{IV}[TpCF_3PP]Cl_2$ and $Pt^{IV}[TpCF_3PC](Ar)(py)$.

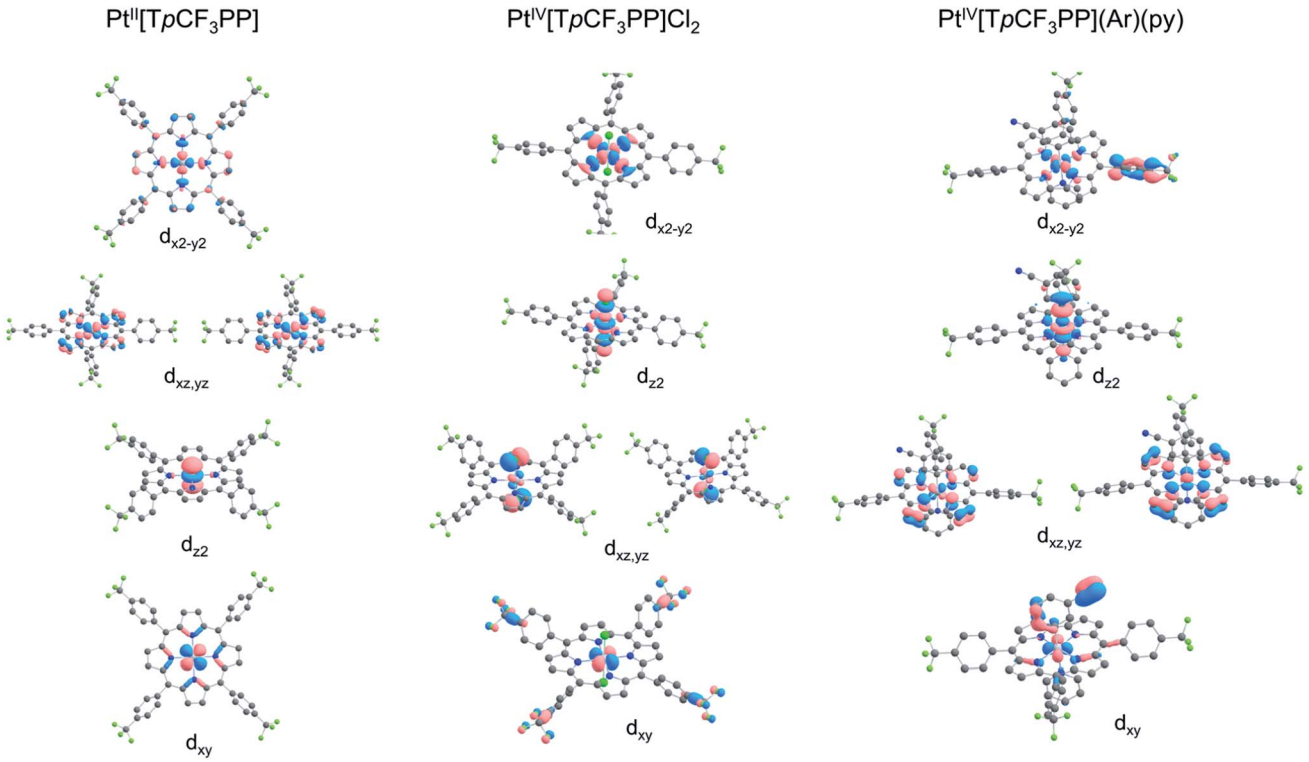

Fig. 6 Platinum 5d-based FMOs of the complexes studied.

species, they occur at slightly different orbital energies. Thus, the d_{xy} orbital has a slightly higher orbital energy (by ~1 eV) in $Pt^{IV}[TpCF_3PC](Ar)(py)$ relative to $Pt^{IV}[TpCF_3PP]Cl_2$. The difference appears to be related to the decrease in symmetry in $Pt^{IV}[TpCF_3PC](Ar)(py)$, which allows the orbital, which is strictly non-bonding in $Pt^{IV}[TpCF_3PP]Cl_2$, to engage in weak σ/σ^* interactions. The (d_{xz}, d_{yz}) pair shown in Fig. 5 exhibits the opposite behavior, with these orbitals lying slightly lower in energy (~0.3 eV) in $Pt^{IV}[TpCF_3PC](Ar)(py)$ compared to $Pt^{IV}[TpCF_3PP]Cl_2$, indicating the combined effects of a number of interactions, especially the π-antibonding interactions with the chlorido ligands. Finally, the d_{z^2} and $d_{x^2-y^2}$ orbitals appear at higher energies (~1.3 and 1.2 eV, respectively) in $Pt^{IV}[TpCF_3PC](Ar)(py)$, as expected for the higher σ-donating abilities of both the equatorial corrole and axial aryl and pyridine ligands and consistent with the higher Pt L_3-edge energy in $Pt^{IV}[TpCF_3PC](Ar)(py)$.

Conclusion

A combined XAS and DFT study of a set of three well-characterized Pt porphyroind complexes has shed light on the factors affecting Pt L_3 pre-edge energies. From $Pt^{II}[TpCF_3PP]$ to $Pt^{IV}[TpCF_3PP]Cl_2$, the Pt L_3 pre-edge energy upshifts by 1.2 V, which is unexpectedly small for a two-electron oxidation of the metal. An explanation comes from DFT calculations, which showed that the oxidation is far from purely metal-centered; instead, the porphyrin ligand in $Pt^{IV}[TpCF_3PP]Cl_2$ is substantially oxidized. From $Pt^{IV}[TpCF_3PP]Cl_2$ to $Pt^{IV}[TpCF_3PC](Ar)(py)$, the Pt L_3 pre-edge energy upshifts by a further 0.4 eV. This upshift is largely attributable to an increase in overall ligand field strength in $Pt^{IV}[TpCF_3PC](Ar)(py)$.

Experimental section

Materials and instruments

Benzonitrile was pre-dried over and distilled from P_4O_{10} and stored over activated 4 Å molecular sieves. Ultraviolet-visible (UV-vis) spectra were recorded on an HP 8454 spectrophotometer in CH_2Cl_2. ^1H (400 MHz) and ^{19}F (376 MHz) NMR spectra were acquired on a 400 MHz Bruker Avance III HD spectrometer equipped with a 5 mm SmartProbe BB/1H (BB = ^{19}F, ^{31}P-^{15}N) in $CDCl_3$ and referenced to $CHCl_3$ (δ = 7.26 ppm) for ^1H and to 2,2,2-trifluoroethanol-d_3 (δ = −77.8 ppm) for ^{19}F. High resolution electrospray ionization mass spectra (HRMS) were recorded on an LTQ Orbitrap XL spectrometer.

Syntheses

$Pt^{II}[TpCF_3PP]$ was synthesized according to Buchler *et al.*[10] by refluxing free-base *meso*-tetra(4-trifluoromethylphenyl) porphyrin with $PtCl_2$ (3 equiv.) in dry benzonitrile for 2.5 h.[38] Purification of the crude product was performed *via* column chromatography on silica gel with *n*-hexane/CH_2Cl_2 as eluent. Subsequent crystallization from 1 : 2 $CHCl_3$/MeOH yielded the desired product as an orange-red solid. Spectroscopic data obtained for $Pt^{II}[TpCF_3PP]$ matched those reported earlier.[39] $Pt^{IV}[TpCF_3PC](Ar)(py)$ was also synthesized as reported recently.[13]

$Pt^{IV}[TpCF_3PP]Cl_2$ was prepared according to Mink *et al.*,[40] with a few modifications, as follows: a saturated solution $Cl_2(g)$ in $CHCl_3$ (1 mL) solution was added dropwise over 2 min to a stirred, chilled (0 °C) solution of $Pt^{II}[TpCF_3PP]$ (40 mg, 0.037 mmol) in $CHCl_3$ (5 mL). The orange solution thereupon turned red and was stirred for an additional 20 min at room temperature. UV-vis spectroscopy at this point showed that $Pt^{II}[TpCF_3PP]$ was still not fully consumed. An additional 1 mL of saturated $Cl_2/CHCl_3$ solution was accordingly added dropwise and the reaction mixture was stirred for a further 40 min, whereupon the 399 nm soret band of $Pt[TpCF_3PP]$ disappeared completely. The dark red solution was evaporated under vacuum and the distillate, essentially $Cl_2/CHCl_3$, was dechlorinated with a saturated aqueous solution of sodium thiosulfate ($Na_2S_2O_3$) prior to disposal. The residue was redissolved in a minimum volume of $CHCl_3$ and the resulting solution was layered with three times its volume of cold MeOH. After 3 days, $Pt^{IV}[TpCF_3PP]Cl_2$ was obtained as shiny, purple crystals (31 mg, 0.021 mmol, 73%). UV-vis λ_{max} [nm, $\varepsilon \times 10^4$ (M^{-1} cm^{-1})]: 324 (2.22), 420 (27.82), 536 (2.21), 600 (0.44). ^1H NMR δ ($CDCl_3$, δ = 7.26 ppm): 9.05 (s, 8H, β-H); 8.42 (d, 8H, J = 8.0 Hz, 5,10,15,20-*o* or -*m*, *p*CF_3Ph); 8.11 (d, 8H, J = 8.0 Hz, *m* or *o*,*p*CF_3Ph) ^{19}F NMR δ: −62.63 (s, 12F, 5,10,15,20-*p*CF_3Ph). HRMS (ESI, major isotopomer) $[M]^+$: 1150.0842 (expt), 1150.0825 (calcd); $[M - 2Cl]^+$: 1079.1475 (expt), 1079.1455 (calcd).

X-ray absorption spectroscopy

The Pt L_3-edge X-ray absorption spectra of the three complexes of interest were measured at the Stanford Synchrotron Radiation Lightsource (SSRL) on the unfocused 20-pole 2 T wiggler sidestation beamline 7–3 under nonstandard ring conditions of 3 GeV and ∼100 mA (low-alpha operations mode at SSRL). An Si(220) double crystal monochromator was used for energy selection. A Rh-coated harmonic rejection mirror was used on beamline 7–3 to reject components of higher harmonics. The monochromator was further detuned by 50% to eliminate components of higher harmonics. All species were ground with boron nitride (BN) as a dilutant and then placed in 1 mm aluminum spacer for solid-state analysis. During data collection, the samples were maintained at a constant temperature of ∼10–15 K using an Oxford Instruments CF 1208 liquid helium cryostat. Data were collected to $k = 14$ $Å^{-1}$ using an ionization chamber detector placed directly downstream of the sample. Internal energy calibration was accomplished *via* simultaneous measurement of the absorption of a Pt foil placed between two ionization chambers situated after the sample. The first inflection point of the foil spectrum was fixed at 11 563.7 eV. No visual change in the rising-edge energy was observed over successive scans, indicating that the samples survived photoreduction/damage under experimental conditions. The data presented here are averages over 2 to 4 scans. The data were processed in the Athena utility of the Demeter 0.9.26 package[41] by fitting a second order polynomial to the pre-edge region and subtracting this from the entire spectrum as background. A three-region spline of orders 2, 3, and 3 was used to model the smoothly decaying post-edge region.

Theoretical EXAFS signals $\chi(k)$ were calculated by using FEFF[42–44] (Macintosh version 8.4). Structural models were obtained from crystal structures. The input structures were successful in generating reasonable phase and amplitude parameters required to obtain a good fit. Data fitting was performed in Artemis utility in the Demeter version 0.9.26 code.[41] The structural parameters varied during the fitting process were the bond distance (R) and the bond variance σ^2, which is related to the Debye–Waller factor resulting from thermal motion, and static disorder of the absorbing and scattering atoms. The nonstructural parameter ΔE_0 (E_0 is the energy at which $k = 0$) was also allowed to vary but was restricted to a common value for every component within a given fit. Coordination numbers were systematically varied in the course of the fits but were fixed within a given fit.

Computational details

All DFT calculations were performed using ORCA 3.0.3,[45] the TPSS *meta*-GGA functional, Pantazi and Neese's SARC-ZORA basis set on Pt[34] and Ahlrich's all-electron def2-TZVP basis set on all other atoms.[35–37]

Conflicts of interest

There are no conflicts to declare.

Acknowledgements

This research was supported in part by grants 262229 and 324139 to AG from the Research Council of Norway. The Stanford Synchrotron Radiation Lightsource, SLAC National Accelerator Laboratory, is supported by the U.S. Department of Energy, Office of Science, Office of Basic Energy Sciences under Contract No. DE-AC02-76SF00515. The SSRL Structural Molecular Biology Program is supported by the DOE Office of Biological and Environmental Research, and by the National Institutes of Health, National Institute of General Medical Sciences (including P41GM103393). The contents of this publication are solely the responsibility of the authors and do not necessarily represent the official views of NIGMS or NIH.

References

1 D. McDonald and L. B. Hunt, *A History of Platinum and its Allied Metals*, Johnson Matthey, London, 1982, p. 450.
2 G. Pinto, *J. Chem. Educ.*, 2017, **94**, 970–975.
3 B. Rosenberg, L. van Camp and T. Krigas, *Nature*, 1965, **205**, 698–699.
4 L. Kelland, *Nat. Rev. Cancer*, 2007, **7**, 573–584.
5 S. Rottenberg, C. Disler and P. Perego, *Nat. Rev. Cancer*, 2021, **21**, 37–50.
6 Z. Wang, Z. Deng and G. Zhu, *Dalton Trans.*, 2019, **48**, 2536–2544.
7 M. Gouterman, in *The Porphyrins*, ed. D. Dolphin, Academic Press, New York, 1978, pp. 1–165.

8 J. Kavandi, J. Callis, M. Gouterman, G. Khalil, D. Wright, E. Green, D. Burns and B. McLachlan, *Rev. Sci. Instrum.*, 1990, **61**, 3340–3347.
9 For a historical account, see: A. Ghosh, *Angew. Chem., Int. Ed.*, 2021, **60**, 9760–9770.
10 J. W. Buchler, K.-L. Lay and H. Stoppa, *Z. Naturforsch., B: Anorg. Chem., Org. Chem.*, 1980, **35**, 433–438.
11 D. Kim, D. Holten, M. Gouterman and J. W. Buchler, *J. Am. Chem. Soc.*, 1984, **106**, 4015–4017.
12 A. B. Alemayehu, H. Vazquez-Lima, C. M. Beavers, K. J. Gagnon, J. Bendix and A. Ghosh, *Chem. Commun.*, 2014, **50**, 11093–11096.
13 A. B. Alemayehu, L. J. McCormick, K. J. Gagnon, S. M. Borisov and A. Ghosh, *ACS Omega*, 2018, **3**, 9360–9368.
14 A. B. Alemayehu, K. E. Thomas, R. F. Einrem and A. Ghosh, *Acc. Chem. Res.*, 2021, **54**, 3095–3107.
15 R. Sarangi, *Coord. Chem. Rev.*, 2013, **257**, 459–472.
16 *X-Ray Absorption and X-Ray Emission Spectroscopy: Theory and Applications*, ed. J. A. van Bokhoven and C. Lamberti, Wiley, New York, 2016, p. 895.
17 A. M. Gänzler, M. Casapu, P. Vernoux, S. Loridant, F. J. Cadete Santos Aires, T. Epicier, B. Betz, R. Hoyer and J.-D. Grunwaldt, *Angew. Chem., Int. Ed.*, 2017, **56**, 13078–13082.
18 T. J. P. Hersbach, A. C. Garcia, T. Kroll, D. Sokaras, M. T. M. Koper and A. T. Garcia-Esparza, *ACS Catal.*, 2021, **11**, 9904–9915.
19 A. A. Hummer and A. Rompel, *Metallomics*, 2013, **5**, 597–614.
20 R. Cao, K. E. Thomas, A. Ghosh and R. Sarangi, *RSC Adv.*, 2020, **10**, 20572–20578.
21 S. Ganguly, L. J. McCormick, J. Conradie, K. J. Gagnon, R. Sarangi and A. Ghosh, *Inorg. Chem.*, 2018, **57**, 9656–9669.
22 R. K. Hocking, S. DeBeer George, Z. Gross, F. A. Walker, K. O. Hodgson, B. Hedman and E. I. Solomon, *Inorg. Chem.*, 2009, **48**, 1678–1688.
23 J. J. Yan, T. Kroll, M. L. Baker, S. A. Wilson, R. Decréau, M. Lundberg, D. Sokaras, P. Glatzel, B. Hedman, K. O. Hodgson and E. I. Solomon, *Proc. Natl. Acad. Sci. U. S. A.*, 2019, **116**, 2854–2859.
24 S. Ganguly, J. Conradie, J. Bendix, K. J. Gagnon, L. J. McCormick and A. Ghosh, *J. Phys. Chem. A*, 2017, **121**, 9589–9598.
25 S. Ganguly, L. J. Giles, K. E. Thomas, R. Sarangi and A. Ghosh, *Chem.–Eur. J.*, 2017, **23**, 15098–15106.
26 J. H. Palmer and K. M. Lancaster, *Inorg. Chem.*, 2012, **51**, 12473–12482.
27 H. Lim, K. E. Thomas, B. Hedman, K. O. Hodgson, A. Ghosh and E. I. Solomon, *Inorg. Chem.*, 2019, **58**, 6722–6730.
28 R. Sarangi, L. J. Giles, K. E. Thomas and A. Ghosh, *Eur. J. Inorg. Chem.*, 2016, 3225–3227.
29 S. Ganguly and A. Ghosh, *Acc. Chem. Res.*, 2019, **52**, 2003–2014.
30 J. Herritsch, J.-N. Luy, S. Rohlf, M. Gruber, B. P. Klein, M. Kalläne, P. Schweyen, M. Bröring, K. Rossnagel, R. Tonner and J. M. Gottfried, *ECS J. Solid State Sci. Technol.*, 2020, **9**, 061005.
31 J. A. Horsley, *J. Chem. Phys.*, 1982, **76**, 1451–1458.
32 A. N. Mansour, J. W. Cook Jr and D. E. Sayers, *J. Phys. Chem.*, 1984, **88**, 2330–2334.
33 J. Tao, J. P. Perdew, V. N. Staroverov and G. E. Scuseria, *Phys. Rev. Lett.*, 2003, **91**, 146401.
34 D. A. Pantazis, X.-Y. Chen, C. R. Landis and F. Neese, *J. Chem. Theory Comput.*, 2008, **4**, 908–919.
35 A. Schaefer, H. Horn and R. Ahlrichs, *J. Chem. Phys.*, 1992, **97**, 2571–2577.
36 A. Schaefer, C. Huber and R. Ahlrichs, *J. Chem. Phys.*, 1994, **100**, 5829–5835.
37 F. Weigend and R. Ahlrichs, *Phys. Chem. Chem. Phys.*, 2005, **7**, 3297–3305.
38 R. C. Kwong, S. Sibley, T. Dubovoy, M. Baldo, S. R. Forrest and M. E. Thompson, *Chem. Mater.*, 1999, **11**, 3709–3713.
39 C. Arunkumar, F. R. Kooriyaden, X. Zhang, S. Sujatha and J. Zhao, *New J. Chem.*, 2017, **41**, 4908–4917.
40 L. M. Mink, M. L. Neitzel, L. M. Bellomy, R. E. Falvo, R. K. Boggess, B. T. Trainum and P. Yeaman, *Polyhedron*, 1997, **16**(16), 2809–2817.
41 B. Ravel and M. Newville, *J. Synchrotron Radiat.*, 2005, **12**, 537–541.
42 J. Mustre de Leon, J. J. Rehr, S. I. Zabinsky and R. C. Albers, *Phys. Rev. B: Condens. Matter Mater. Phys.*, 1991, **44**, 4146–4156.
43 J. J. Rehr, J. Mustre de Leon, S. I. Zabinsky and R. C. Albers, *J. Am. Chem. Soc.*, 1991, **113**, 5135–5140.
44 S. I. Zabinsky, J. J. Rehr, A. Ankudinov, R. C. Albers and M. J. Eller, *Phys. Rev. B: Condens. Matter Mater. Phys.*, 1995, **52**, 2995–3009.
45 F. Neese, *ORCA: An ab initio, DFT and semiempirical SCF-MO package*, Version 3.0.1, University of Bonn, Germany, 2013.